Fusion of B-mode and shear wave elastography ultrasound features for automated detection of axillary lymph node metastasis in breast carcinoma

PHAM, The-Hanh, FAUST, Oliver <http://orcid.org/0000-0002-3979-4077>, KOH, Joel En Wei, CIACCIO, Edward J., BARUA, Prabal D., OMAR, Norlia, NG, Wei Lin, AB MUMIN, Nazimah <http://orcid.org/0000-0001-8720-5700>, RAHMAT, Kartini and ACHARYA, U. Rajendra <http://orcid.org/0000-0003-2689-8552>

Published version

PHAM, The-Hanh, FAUST, Oliver, KOH, Joel En Wei, CIACCIO, Edward J., BARUA, Prabal D., OMAR, Norlia, NG, Wei Lin, AB MUMIN, Nazimah, RAHMAT, Kartini and ACHARYA, U. Rajendra (2022). Fusion of B-mode and shear wave elastography ultrasound features for automated detection of axillary lymph node metastasis in breast carcinoma. Expert Systems.

Copyright and re-use policy

Received: 18 July 2021 | Accepted: 10 January 2022

DOI: 10.1111/exsy.12947

ORIGINAL ARTICLE

Expert Systems WILEY

Fusion of B-mode and shear wave elastography ultrasound features for automated detection of axillary lymph node metastasis in breast carcinoma

The-Hanh Pham[1] | Oliver Faust[2] | Joel En Wei Koh[1] | Edward J. Ciaccio[3] | Prabal D. Barua[4] | Norlia Omar[5] | Wei Lin Ng[5] | Nazimah Ab Mumin[5,6] | Kartini Rahmat[5] | U. Rajendra Acharya[1,5,7,8]

[1]School of Engineering, Ngee Ann Polytechnic, Singapore, Singapore

[2]Department of Engineering and Mathematics, Sheffield Hallam University, Sheffield, UK

[3]Department of Medicine, Columbia University, New York, New York, USA

[4]School of Management and Enterprise, University of Southern Queensland, Toowoomba, Queensland, Australia

[5]Department of Biomedical Imaging, Faculty of Medicine, University of Malaya, Kuala Lumpur, Malaysia

[6]Radiology Department, Faculty of Medicine, University Teknologi MARA, Sungai Buloh Campus, Sungai Buloh, Malaysia

[7]School of Science and Technology, Singapore University of Social Sciences, Singapore, Singapore

[8]Department of Bioinformatics and Medical Engineering, Asia University, Taichung, Taiwan

Correspondence
U. Rajendra Acharya, Department of Electronics and Computer Engineering, Ngee Ann Polytechnic, Clementi Road, Singapore 599489, Singapore.
Email: aru@np.edu.sg

Funding information
University of Malaya Faculty Research Grant (RU Grant-Faculty Programme), Grant/Award Number: FP017-2019; Fundamental Research Grant Scheme, Grant/Award Number: GPF06C-2018

Abstract

In this study, we evaluate and compare the diagnostic performance of ultrasound for non-invasive axillary lymph node (ALN) metastasis detection. The study was based on fusing shear wave elastography (SWE) and B-mode ultrasonography (USG) images. These images were subjected to pre-processing and feature extraction, based on bi-dimensional empirical mode decomposition and higher order spectra methods. The resulting nonlinear features were ranked according to their *p*-value, which was established with Student's *t*-test. The ranked features were used to train and test six classification algorithms with 10-fold cross-validation. Initially, we considered B-mode USG images in isolation. A probabilistic neural network (PNN) classifier was able to discriminate positive from negative cases with an accuracy of 74.77% using 15 features. Subsequently, only SWE images were used and as before, the PNN classifier delivered the best result with an accuracy of 87.85% based on 47 features. Finally, we combined SWE and B-mode USG images. Again, the PNN classifier delivered the best result with an accuracy of 89.72% based on 71 features. These three tests indicate that SWE images contain more diagnostically relevant information when compared with B-mode USG. Furthermore, there is scope in fusing SWE and B-mode USG to improve non-invasive ALN metastasis detection.

KEYWORDS
axillary lymph node, cancer detection, higher order spectra, machine learning, shear wave elastography, ultrasound

1 | INTRODUCTION

The incidence of breast cancer is the second most common among women (Siegel et al., 2019). Breast cancer often metastasizes to the axillary lymph node (ALN). The role of analysis of ALN is important as it provides a reliable prognosis in staging breast cancers leading to early treatment

and intervention (Goldhirsch et al., 2011). Current clinical pathways for ALN metastasis detection are structured as follows. All patients will undergo pre-operative ultrasound of the axillary region to detect lymph nodes. If it is suspicious, fine needle aspiration or ultrasound guided core biopsy will be performed for histopathological confirmation. A sentinel lymph node biopsy (SLNB) is suggested if B-mode ultrasonography (USG) features are not suspicious and in suspicious cases if the histopathology result shows no evidence of metastatic nodal involvement. If histopathology results or B-mode USG strongly indicates malignant involvement, then axillary lymph node dissection (ALND) is recommended (Amanti et al., 2009; Van la Parra et al., 2009). As such, this pathway indicates that the accuracy of ultrasound scans is insufficient when it comes to identifying involved lymph nodes (Fernández et al., 2011; Mainiero et al., 2010). Ultrasound methods are especially unreliable for patients with early stage breast cancer (Evans et al., 2014; Lee et al., 2013). Ultrasound guided core biopsy, SLNB, and ALND are invasive and these methods expose patients to considerable risk (della Rovere et al., 2006; Giuliano et al., 2011; Wu & Burstein, 2004). Hence, there is a need to find a reliable non-invasive method for inferring the ALN status prior to invasive interventions, such as surgery. Such a method might improve early stage breast cancer management.

Ultrasound is one of the readily available, non-invasive imaging techniques currently utilized in clinical pathways for ALN metastasis detection. It is a relatively simple and quick method which does not expose patients to radiation. Hence, focusing on improving the diagnostic relevance of ultrasound scanning is one way to resolve the problem of non-invasive ALN metastasis detection. Standard methods for ultrasound-based ALN metastasis detection involve analysing morphological characteristics of images captured during scans. For example, radiologists look for the presence of cortical thickening and loss of fatty hilum (Alvarez et al., 2006; Ecanow et al., 2013; Tamaki, Tamaki, Kamada, Uehara, Miyashita, Chan, et al., 2013). Unfortunately, the sensitivity of standard methods is low for non-palpable ALN studies (Choi et al., 2011; Coutant et al., 2009). Another method that can be used for metastasis detection in organs is ultrasound elastography. This method can provide information about the stiffness of lesions (Choi et al., 2011; Evans et al., 2014; Tamaki, Tamaki, Kamada, Uehara, Miyashita, Ishida, & Sasano, 2013). Shear wave elastography (SWE) is a widely used non-invasive medical imaging technique to measure tissue elasticity. Studies have shown that it can be used to differentiate between benign and malignant breast lesions (Kilic et al., 2016; Luo et al., 2019). Recently the method has also been applied to ALN metastasis detection in clinical settings (Ng et al., 2021; Seo & Sohn, 2018; Youk et al., 2017). The potential of this method was also recognized by the American College of Radiology (ACR), who included SWE in the 5th edition of their Breast Imaging Reporting and Data System (BI-RADS) lexicon (Acharya, Ng, et al., 2017; American College of Radiology and D'Orsi, Carl J, 2013; Berg et al., 2012; Evans et al., 2012; Ng et al., 2016; Olgun et al., 2014). Having two ultrasound-based methods for ALN metastasis detection raises the question on which method is better or indeed which method should be used as part of the clinical pathway. Furthermore, as it may not be an either/or question, we need to investigate whether there is scope in fusing the information captured with both methods to improve ALN metastasis detection.

With this study, we put forward the hypothesis that ultrasound imagery, captured with current technology, contains sufficient information to improve the diagnostic quality of ALN metastasis detection. To test this hypothesis, we have evaluated the detection rate of SWE for differentiating non-metastatic from metastatic ALN in breast cancer patients. Subsequently the results were compared with the findings established by B-mode USG parameters for the same problem. The comparative study was established with a sophisticated information extraction system, based on feature engineering and machine classification. We have used bi-dimensional empirical mode decomposition (BEMD) and higher order spectra (HOS) to extract nonlinear features which capture the subtle pixel changes that indicate malignant involvement. The features were used to train and test a range of classification algorithms. This system distilled a label, either positive or negative, from B-mode USG and SWE ALN ultrasound imagery. A positive label indicates that metastasis is present, and a negative label indicates its absence. Comparing these labels with ground truth, established by clinical experts, enabled us to determine the accuracy, sensitivity, and specificity of the information extraction system. We found that an information extraction system based on B-mode USG imagery with probabilistic neural network (PNN) classification achieved an Accuracy (ACC) of 74.77%, Sensitivity (SEN) of 64.00%, and Specificity (SPE) of 84.21%. For SWE imagery, the same classifier achieved ACC of 87.85%, SEN of 88.00%, and SPE of 87.72%. For a final test, we combined the most significant features from both B-mode USG and SWE. With the combined features, the PNN classifier achieved ACC of 89.72%, SEN of 84.00%, and SPE of 94.74%. We learned that SWE-based diagnosis support is more relevant than B-mode USG-based support. Furthermore, there is scope in fusing the information from SWE and B-mode USG to improve the reliability of ultrasound-based ALN metastasis detection. To the best of our knowledge, this is the first work on automated ALN detection which fuses shear wave and B-mode ultrasound to improve the breast cancer detection quality.

To support our hypothesis, we have structured the remainder of this article as follows. Section 2 introduces the study methods. These methods were used to implement and test the sophisticated information extraction system. As such, Section 3 provides the test results. These results constitute feedback for the wider research community, as discussed in Section 4. The last section provides a summary and concluding remarks.

2 | METHODS

In this section, we describe the methods used to construct a processing system that determines if an ultrasound image shows ALN metastasis. The system design incorporates feature engineering, classification, and quality assessment. The basic idea, which helped to resolve the design

choices, unfolds as follows. We use pre-processing to create the same image type for both B-mode USG and SWE raw images. After that unification, we proceed with feature engineering. That involves feature extraction and feature selection. Once the features are selected, we form feature vectors to train and test the classification algorithms. As such, we have tested six algorithms, namely: support vector machine (SVM), decision tree (DT), K-nearest neighbour (K-NN), PNN, linear discriminant analysis (LDA), and quadratic discriminant analysis (QDA). The performance of these algorithms was established by comparing the test results with ground truth created by human experts through a medical diagnostic process. This ground truth was provided in the form of labels which accompany the raw ultrasound images.

Figure 1 shows an overview diagram of the information extraction system. The diagram depicts two data sources, one for B-mode USG imagery and one for SWE imagery. Next, the data is pre-processed and subjected to BEMD. Radon transformation and HOS techniques were used for feature extraction. The resulting features were grouped into three sets. The first set contained features extracted from B-mode USG images, the second set contained features from SWE images, and the third set contained the features from both B-mode USG + SWE images. Thereafter, Student's *t*-test was utilized to rank the features in each set. Once the features were ranked, they were used to train and test the six classification algorithms with 10-fold cross-validation. The number of features (NoF) was established based on the best classification performance. As a result, we established the information content of B-mode USG images, SWE images, and a combination of B-mode USG + SWE images based on an objective measure for classification performance. The sections below describe the individual methods in more detail.

2.1 | Data

The ultrasound images that were used as data for this study were from patients referred from the Department of Surgery, University Malaya Medical Centre between August 2018 to December 2019. This study was approved by the institution's Medical Ethics Committee (MECID No: 201879-6469). Written informed consent were obtained from the patients.

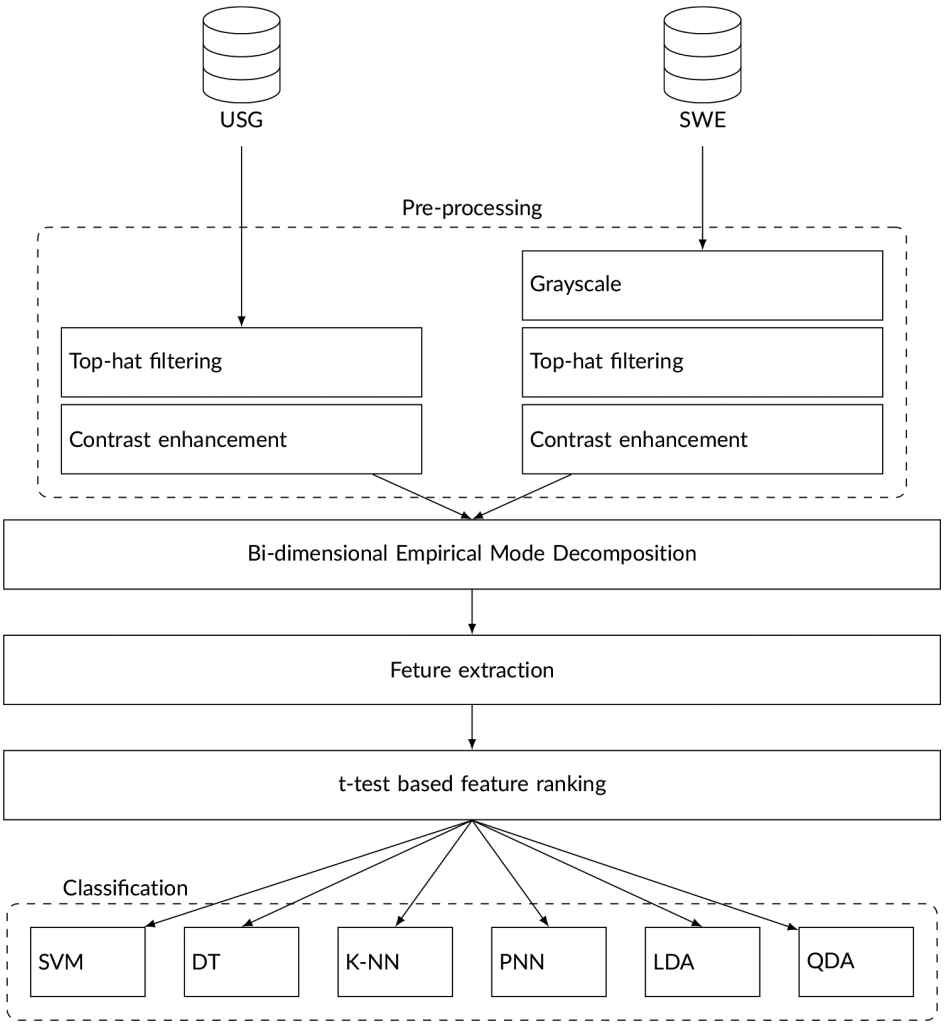

FIGURE 1 Overview block diagram

Ultrasound images were collected from 107 patients who underwent pre-operative assessment due to suspicious breast lesions (BI-RADS 5 and above). Two images of the same ALN were taken from each patient: one SWE and one B-mode USG. Both histopathological analysis and ultrasound imaging were used by radiologists to diagnose ALN metastasis:

1. Negative: 57 patients without metastasis.
2. Positive: 50 patients with metastasis.

The ultrasound (US) images were taken using Aixplorer ultrasound system (SuperSonic Imagine). A transducer with a linear operation range between 4 and 15 MHz was used during the scans. Two radiologists with 5- and 15-years of experience carried out the scans. Prior to the measurements, they underwent a 1-month training course which helped them to familiarize with the SWE method. Special emphasis was placed on both detecting and analysing ALNs. The histological diagnosis results were only disclosed after the analysis and detection tasks were completed.

During the B-mode USG scans, the patients were in the supine position with their arms placed above the head. Two orthogonal planes were taken for breast lesions. Three-dimensional (3D) measurements and colour Doppler were recorded. One image plane was taken for ALN detection and the short axis diameter was recorded. Loss of fatty hilum and cortical thickening, with a cut-off point of >3 mm, were used as indicators to establish a suspicion that metastasis is present.

SWE was performed on the most suspicious ALNs as determined by B-mode USG. As such, the 'most suspicious ALN' was defined as the ALN that exhibited loss of fatty hilum or eccentric cortical thickening. Patients were required to hold their breath while the radiologist held the ultrasound probe for 10 s for the production of shear waves. A region of interest (ROI) circular box of the system (Q-box SuperSonic Imagine) was placed at the stiffest region of the breast lesion and ALN (including the perilesional stiff tissue) (Youk et al., 2017). A standardized size of Q-box diameter which included 3 mm for breast lesion and 1–2 mm for ALN were used (Luo et al., 2019; Tourasse et al., 2012). Quantitative values within ROI included the mean (E mean), maximum (E max), minimum (E min), elasticity ratio (E ratio), and standard deviation (E SD) of elasticity values, defined in kPa.

Quantitative assessment of SWE images were performed using colour patterns based on a colour elastic map, adapted from Luo et al. (2019). The colour patterns were defined as follows: Colour Pattern 1: homogeneous pattern of ALN; Colour Pattern 2: filling defect within ALN; Colour Pattern 3: homogeneous within ALN with localized coloured area at the margin; and, Colour Pattern 4: filling defect within ALN with a localized coloured area at the margin.

2.1.1 | Histopathological analysis

Gold standard assessment was histopathological results taken from surgical specimens of SLNB or ALND. The results showed non metastatic or metastatic disease.

2.2 | Pre-processing

The objective for the pre-processing algorithms was to prepare the ultrasound imagery for feature extraction. The first step was to harmonize the raw data through greyscaling the SWE images. Thereafter, the images were processed by top-hat filtering and contrast enhancement. The following paragraphs detail the methods used.

2.2.1 | Greyscale

This pre-processing technique uses colorimetry to calculate the grayscale values for the SWE images (Saravanan, 2010). The grayscale algorithm makes SWE images similar to B-mode USG images and after that step, both image types can be processed with the same algorithms. Unfortunately, colour information is lost in the process of transferring SWE images to grayscale.

2.2.2 | Top-hat filtering

That operation extracts small elements and details from the harmonized ultrasound images (Coster & Chermant, 2001). There exist two types of top-hat transform: the white top-hat transform is defined as the difference between the input image and its opening by some structuring element, while the black top-hat transform is defined dually as the difference between the closing and the input image.

2.2.3 | Contrast enhancement

Adaptive histogram equalization was used to improve the top-hat filtered image contrast. That is achieved by changing each grayscale pixel with a transformation function derived from a neighbourhood region (Pizer et al., 1987). The algorithm used in this study operates on small regions in the image called tiles. The algorithm enhances the contrast of each tile, so that the histogram of the output region approximately matches a specified histogram. Independent operations on individual tiles might introduce artificial boundaries. Bilinear interpolation is used to reduce the tile differences along the boundaries.

2.3 | Bi-dimensional empirical mode decomposition

In this study, we have used BEMD for texture analysis (Faust, Acharya, et al., 2018; Mozaffarilegha et al., 2020), because this method can extract global structure even when fractals are present (Chen & Jeng, 2014). The data was examined in an adaptive time–frequency–amplitude space which accommodates non-linear and non-stationary image texture. The BEMD algorithm decomposes the top-hat filtered ultrasound images into four intrinsic mode functions (IMFs) (Nunes et al., 2005). The second row of images in Figure 2 shows IMF1 for example images. Similarly, rows 3–5 in Figure 2 show IMF2 to IMF4, respectively, for the same example images. As such, the BEMD algorithm is based on a two-dimensional (2D) extension of the empirical mode decomposition, which uses a sifting process which considers the neighbouring windows to detect extrema iteratively (Huang et al., 1998). The sifting process uses the radial basis function (RBF) to connect the maxima and minima points, forming an 'envelope'.

2.4 | Feature extraction

Feature engineering is the art of finding algorithms that extract relevant information from data. For this study, we focused on HOS methods to accomplish that task. We have designed a two-step process that extracts 288 features from each IMF image. Step 1 employs a Radon transform to convert the 2D imagery into one-dimensional (1D) signals (Acharya et al., 2013; Acharya, Meiburger, Faust, et al., 2019; Radon, 1986). The algorithm steps-through a 180° semi-circle with 10° increments. The 18 results are passed on to the second step. Step 2 uses four HOS algorithms to extract four features from these signals (Chandran et al., 1997; Chandran & Elgar, 1991, 1992, 1993; Chua et al., 2010). The four features were normalized bispectrum (HOS entropy), normalized bispectrum squared (HOS entropy2), normalized bispectrum cubic (HOS entropy3), and HOS entropy phase (Nikias & Mendel, 1993). The feature extraction process can be summarized as follows: four IMFs were extracted from each ultrasound image. With the radon transform 18 1D signals were extracted from each IMF. From each 1D signal four HOS features were extracted. Hence, the algorithm chain extracted $288 = 4 \times 18 \times 4$ features for each ultrasound image.

2.5 | *T*-test based feature ranking

A *t*-test seeks to establish that a given statistic follows a Student's *t*-distribution under the null hypothesis (Student, 1908). We have used the *t*-test to determine if the mean of a set which contains the values of a specific feature extracted from all 50 positive samples is significantly different from the mean of a set that contains the values of the same feature, extracted from the 57 negative samples. Our null hypothesis was that both sets have the same mean. The so-called *p*-value is the result of these efforts. As such, this value measures the probability that features extracted from additional US images are similar to the results already observed, based on the assumption that the two classes have no statistical relationship (Murtaugh, 2014). A very small *p*-value means that such an extreme observed outcome would be very unlikely under the null hypothesis. In our study, it meant that features with a lower *p*-value were better in discriminating positive versus negative ALN metastasis cases. Therefore, we ranked the features according to their *p*-value in ascending order. This was done for features extracted from B-mode USG imagery, SWE imagery, and for features extracted from both B-mode USG and SWE imagery.

2.6 | Classification

As part of this study, we have tested the ability of six classifiers to discriminate between positive (metastasis) and negative (normal) ALNs. The classifiers were trained and tested according to the rules of 10-fold cross-validation. The following text describes the data handling for 10-fold cross-validation, and it introduces the individual classification algorithms.

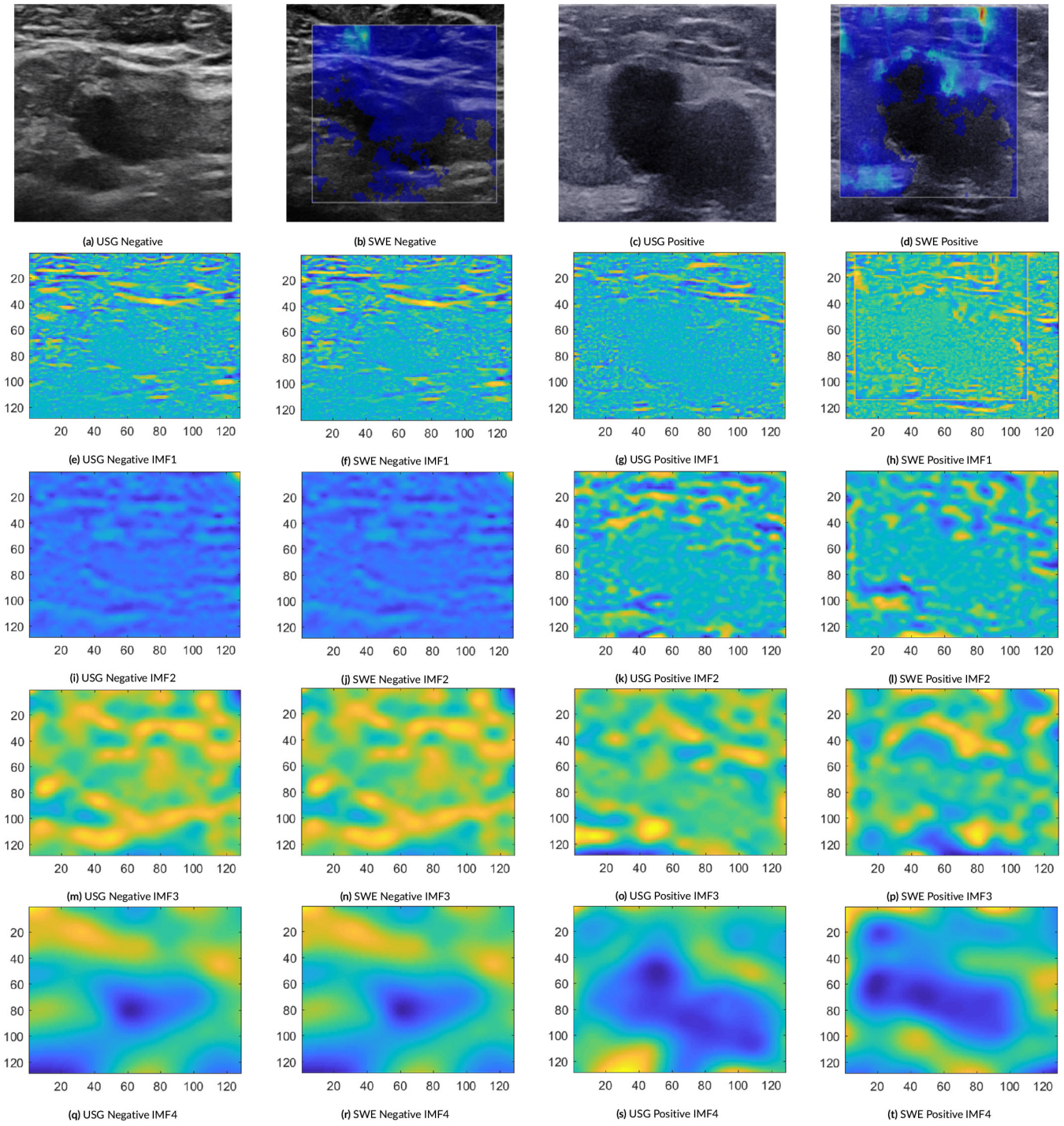

FIGURE 2 Example images, together with their IMF processing, from both positive and negative classes

2.6.1 | Feature vectors

t-test based feature ranking resulted in three ordered sets of features having 288 elements each. We use that information to generate 287 sets of feature vectors for each ordered set of features. The feature vector sets are assembled as follows. The first set contains 107 2D feature vectors, 57 with a negative label and 50 with a positive label. The first element is the most significant feature, and the second element is the second most significant feature. The next set contains 3D feature vectors whose elements are sourced from the three most significant features. This continues until all 287 feature vector sets are created. As such, set 287 contains feature vectors with all 288 features. Each of the $861 = 287 \times 3$ feature vector sets was used to train and test six classification algorithms based on 10-fold cross-validation.

TABLE 1 Partitioning of the feature vector set

	Part									
Feature vector class	**1**	**2**	**3**	**4**	**5**	**6**	**7**	**8**	**9**	**10**
Number of negative feature vectors	5	5	5	6	6	6	6	6	6	6
Number of positive feature vectors	5	5	5	5	5	5	5	5	5	5

2.6.2 | 10-fold cross-validation

This validation method reduces the bias that arises from splitting a dataset into training and testing subsets (Kohavi, 1995). For this study, we had 50 positive and 57 negative feature vectors. In the first step, we have split the available feature vector set into 10 parts. Table 1 provides more details on that split. In a second step, we generated 10 folds as follows: Each of the 10 parts was used for testing and the remaining nine parts were used for training the classification algorithm. The individual classifiers are described below.

2.6.3 | Decision tree

A DT is a classifier can be expressed as a recursive partition of the instance space (Loh, 2011; Rokach & Maimon, 2005). The algorithm creates nodes and assembles them in the form of a rooted tree. The root node has no incoming edges—it sources the data. Internal nodes have one incoming and two outgoing edges. Each internal node decides, based on the input attributes, over which output edge the data is passed. That decision splits the instance space into two sub-spaces. Nodes with only one input are called leaves. These leaves return the classification result—either positive or negative.

2.6.4 | Linear discriminant analysis

In 1936, Fischer proposed LDA. The algorithm computes a projection hyperplane which minimizes the variance between classes while at the same time maximizing the distance between the projected means of the classes. The functionality is based on solving an eigenvalue problem where the corresponding eigenvector defines the hyperplane of interest. We have used the resulting hyperplane as a decision border which establishes a classification system (Balakrishnama & Ganapathiraju, 1998; Izenman, 2013; Xanthopoulos et al., 2013).

2.6.5 | Quadratic discriminant analysis

QDA extends LDA by allowing the intraclass covariance matrices to differ between classes, so that discrimination is based on quadratic rather than on linear functions (Pardoe et al., 2007; Srivastava et al., 2007).

2.6.6 | K-nearest neighbour

The k-nearest-neighbour classifier is commonly based on the Euclidean distance between a test sample and the specified training samples (Kramer, 2013). An object is classified by a plurality vote of its neighbours, with the object being assigned to the class most common among its K-NNs (Altman, 1992).

2.6.7 | Probabilistic neural network

PNNs can be used to solve pattern recognition and classification problems. The PNN algorithm establishes the parent probability distribution function of each class with an approximated Parzen window and a non-parametric function (Mohebali et al., 2020).

2.6.8 | Support vector machine

A SVM constructs a hyperplane in a high-dimensional space, which is used to separate positive and negative cases (Cortes & Vapnik, 1995). The classification quality depends on the separation between the class specific data points. The hyperplane is chosen such that it has the largest distance to the nearest training-data point of any class (so-called functional margin). That minimizes the generalization error of the classifier (Noble, 2006).

3 | RESULTS

In this section, we document the classification and feature selection results. In the previous steps we have extracted the information from raw ultrasound images. The information was captured in feature vectors and these feature vectors were arranged for 10-fold cross-validation. These feature vectors allowed us to investigate the information extracted from B-mode USG, SWE, and B-mode USG + SWE. That investigation took the form of classification-based feature selection. The basic idea was to use every feature vector set to train and test each classification algorithm. Based on the results, we detected the highest accuracy for B-mode USG, SWE, and B-mode USG + SWE. Doing so revealed the classification performance of a specific classification algorithm and the NoF used to achieve that classification performance.

3.1 | B-mode USG results

Table 2 documents the highest accuracy results that were achieved by testing six classification algorithms with feature vectors extracted from B-mode USG imagery. Each row in the table body provides information about NoF, confusion matrix, and classification performance for one of the six classification algorithms. For the binary classification problem of separating positive from negative, the confusion matrix has four entries, namely, True Positive, True Negative, False Positive, and False Negative. The entry values were calculated by rounding the mean result for all folds to the nearest integer. The classification performance was established with ACC, positive predictive value, SEN, and SPE measures. Overall, the best classification performance was achieved by the PNN classifier. That algorithm achieved a classification ACC of 74.77% with the 15 best features.

Figure 3 documents our efforts to train and test the PNN classification algorithm. The graph represents the average accuracy of the algorithm over the NoF in the feature vectors used for training and testing. In this case, average accuracy indicates the mean accuracy for all 10 folds. Purely for display purposes, we limited the NoF to a range of 2–24. The resulting graph has a maximum of 74.80% for 15 features, which corresponds to the highest accuracy achieved for B-mode USG imagery.

3.2 | SWE results

Table 3 documents the highest accuracy results that were achieved by testing six classification algorithms with feature vectors extracted from B-mode USG + SWE imagery. Overall, the best classification performance was achieved by the PNN classifier. That algorithm achieved a classification ACC of 87.85% with the 47 best features.

Figure 4 documents our efforts to train and test the PNN classification algorithm. For display purposes, we limited the NoF to a range of 2–72. The resulting graph has a maximum of 87.85% for 47 features, which corresponds to the highest accuracy achieved for SWE imagery.

3.3 | B-mode USG + SWE results

Table 4 documents the highest accuracy results that were achieved by testing six classification algorithms with feature vectors extracted from B-mode USG + SWE imagery. Overall, the best classification performance was again achieved by the PNN classifier. That algorithm achieved a classification ACC of 89.72% with the 71 best features.

TABLE 2 B-mode USG classification results

Classifier	NoF	TP	TN	FP	FN	ACC	PPV	SEN	SPE
DT	5	32	32	25	18	59.81%	56.14%	64.00%	56.14%
LDA	15	36	39	18	14	70.09%	66.67%	72.00%	68.42%
QDA	2	32	37	20	18	64.49%	61.54%	64.00%	64.91%
K-NN	14	36	41	16	14	71.96%	69.23%	72.00%	71.93%
PNN	15	32	48	9	18	74.77%	78.05%	64.00%	84.21%
SVM	16	32	41	16	18	68.22%	66.67%	64.00%	71.93%

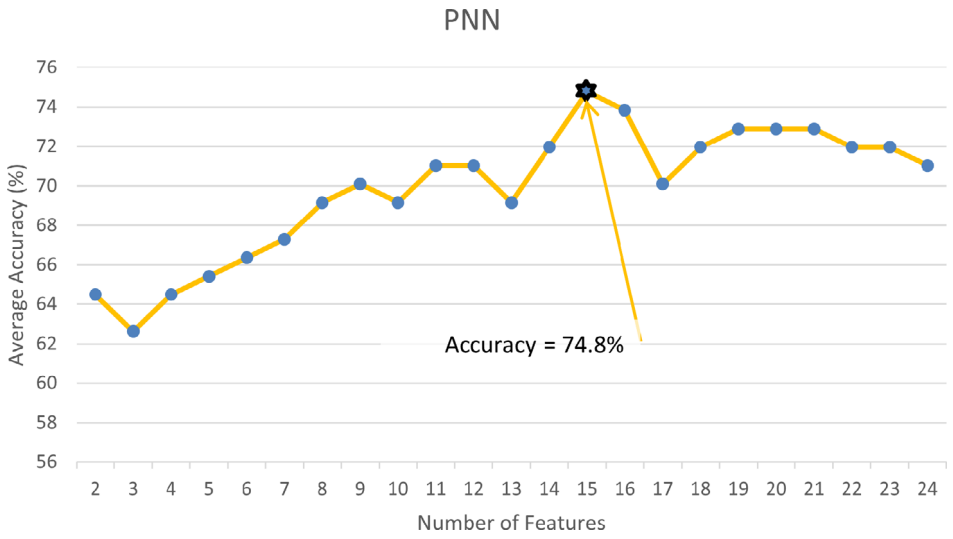

FIGURE 3 Testing the PNN classifier with feature vectors extracted from B-mode USG imagery

TABLE 3 SWE classification results

Classifier	NoF	TP	TN	FP	FN	ACC	PPV	SEN	SPE
DT	17	39	46	11	11	79.44%	78.00%	78.00%	80.70%
LDA	46	40	49	8	10	83.18%	83.33%	80.00%	85.96%
QDA	22	39	50	7	11	83.18%	84.78v	78.00%	87.72%
K-NN	67	43	50	7	7	86.92%	86.00%	86.00%	87.72%
PNN	47	44	50	7	6	87.85%	86.27%	88.00%	87.72%
SVM	41	42	48	9	8	84.11%	82.35%	84.00%	84.21%

Figure 5 documents our efforts to train and test the PNN classification algorithm. For display purposes, we limited the NoF to a range of 2–95. The resulting graph has a maximum of 89.72% for 71 features, which corresponds to the highest accuracy achieved for B-mode USG + SWE imagery.

The 71 features, from B-mode USG + SWE imagery were selected based on the highest accuracy value of 89.72%. Table 5 shows the selected features, starting with the highest rank (1) down to the lowest rank (71). The rank corresponds to the *t*-value where a higher value indicates that the feature was better in discriminating positive from negative cases, which justifies a higher feature rank. Careful analysis of the table shows that 60 of the top features were extracted from SWE images and 11 features were extracted from B-mode USG images. IMF4 was most often selected (34 occurrences), followed by IMF1 (20), IMF3 (11), and IMF2 (6). With 22 occurrences, Bi spectrum Entropy 1 features most prominently in the table, followed Bi spectrum Entropy 3 with 17 occurrences, and Bi spectrum Entropy 2 with 16 occurrences. Phase entropy also occurred 16 times.

4 | DISCUSSION

HOS entropy features are able to capture subtle changes in pixel variation (Acharya, Sudarshan, et al., 2017; Noronha et al., 2014). Hence, they have been used in automated medical image classification (Acharya et al., 2016; Acharya, Meiburger, Koh, et al., 2019; Acharya, Ng, et al., 2017; Koh et al., 2017).

It can be noted from the features demonstrated in Table 5 that most of the HOS-based features have shown higher feature values for the presence of metastatic ALN (positive cases) as compared with the negative class. The presence of metastatic ALNs will cause a sudden change in pixel value. Therefore, pixel value variability increases entropy value.

In addition, it can be noted from our classification results that using B-mode USG alone, our proposed system is able to obtain the highest classification accuracy of 74.77% using 15 features with a PNN classifier. We have obtained a classification accuracy of 87.85% using SWE images with PNN classifier. We have obtained an accuracy of 89.72% using B-mode USG + SWE images with a PNN classifier. Among the

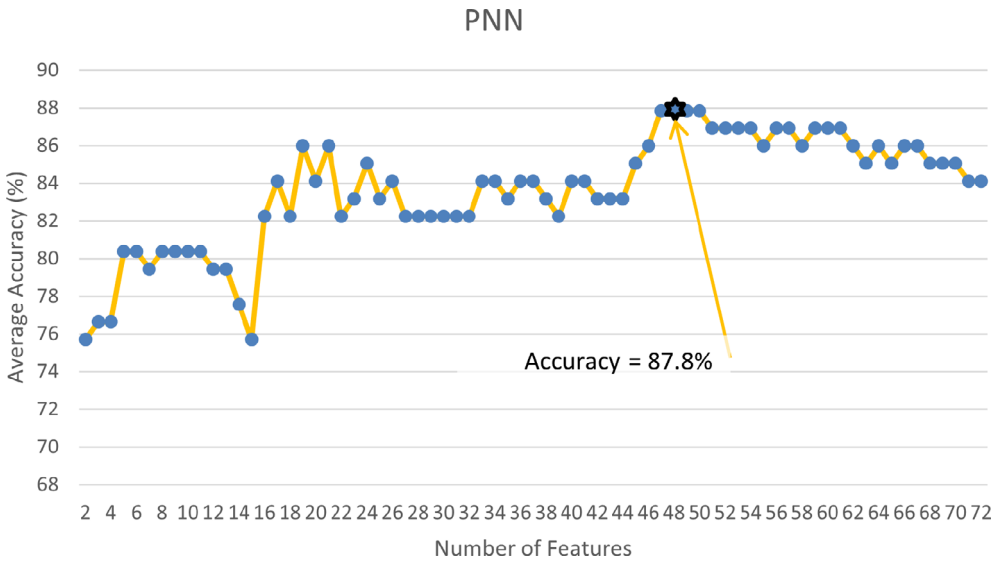

FIGURE 4 Testing the PNN classifier with feature vectors extracted from SWE imagery

TABLE 4 B-mode USG combined with SWE classification results

Classifier	NoF	TP	TN	FP	FN	ACC	PPV	SEN	SPE
DT	26	41	48	9	9	83.18%	82.00%	82.00%	84.21%
LDA	62	40	51	6	10	85.05%	86.96%	80.00%	89.47%
QDA	65	41	51	6	9	85.98%	87.23%	82.00%	89.47%
K-NN	47	44	49	8	6	86.92%	84.62%	88.00%	85.96%
PNN	71	42	54	3	8	89.72%	93.33%	84.00%	94.74%
SVM	20	42	45	12	8	81.31%	77.78%	84.00%	78.95%

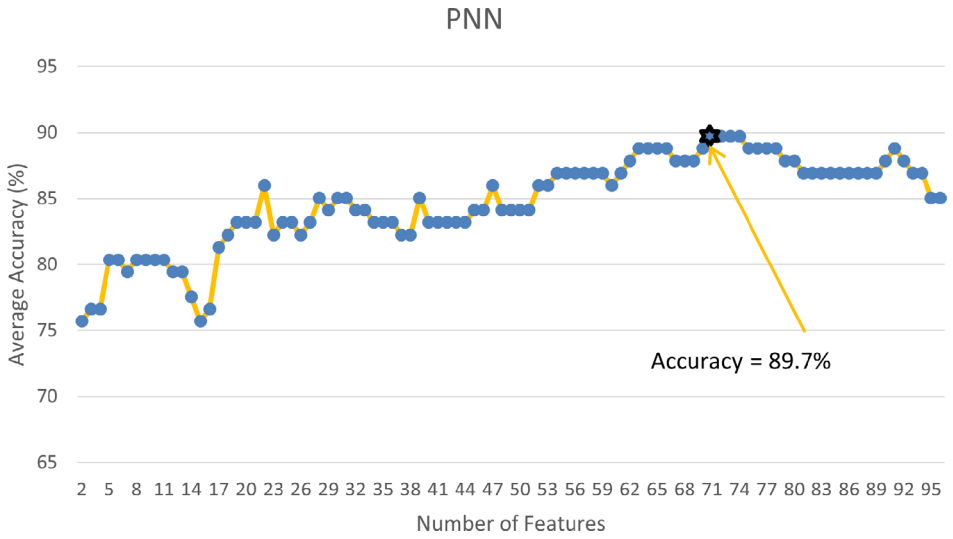

FIGURE 5 Testing the PNN classifier with feature vectors extracted from both B-mode USG and SWE imagery

evaluated classifiers, the PNN classifier has yielded the best performance for this application, which may be due to the use of a RBF kernel function. This nonlinear kernel has helped to obtain a higher classification performance. Both accuracy (2%) and specificity (7%) for automated ALN metastasis detection increase when we fuse information from B-mode USG and SWE images.

TABLE 5 Performance values of the 71 best features extracted from B-mode USG and SWE imagery

		Group negative		Group positive			
N	Feature	Mean	SD	Mean	SD	*p*-value	*t*-value
1	SWE1 BiSE1 10°	0.847927	0.076808	0.923888	0.03241	1.88E-09	6.807523
2	SWE1 BiSE2 10°	0.61826	0.13497	0.767569	0.094954	1.36E-09	6.67782
3	SWE1 BiSE3 10°	0.435029	0.141112	0.608944	0.142851	6.84E-09	6.319104
4	SWE1 BiSE1 100°	0.872225	0.03009	0.900041	0.030305	6.53E-06	4.752766
5	SWE4 BiSE1 10°	0.403328	0.041076	0.439774	0.042439	1.81E-05	4.499065
6	SWE4 BiSE2 10°	0.088062	0.024786	0.111125	0.031896	7.86E-05	4.133957
7	SWE4 BiSE3 10°	0.042613	0.018298	0.059203	0.02451	0.000171	3.922425
8	SWE4 BiSE1 30°	0.384628	0.039689	0.417731	0.047858	0.000204	3.862733
9	SWE1 BiSEPh 10°	3.507566	0.091669	3.414671	0.152417	0.000332	3.754922
10	SWE4 BiSE2 20°	0.057613	0.017584	0.073599	0.026338	0.000473	3.638945
11	SWE4 BiSE2 30°	0.054189	0.018409	0.070209	0.026534	0.000569	3.57997
12	SWE4 BiSE3 30°	0.013447	0.00792	0.020807	0.012519	0.000592	3.576643
13	SWE4 BiSE3 20°	0.021982	0.011088	0.032734	0.018696	0.000648	3.555047
14	SWE4 BiSE1 20°	0.352431	0.037945	0.382998	0.051022	0.000786	3.476107
15	SWE3 BiSEPh 40°	3.30541	0.222354	3.141142	0.287614	0.00151	3.271108
16	USG1 BiSE1 20°	0.782564	0.035649	0.804265	0.034084	0.001731	3.216145
17	SWE1 BiSEPh 80°	3.561141	0.006353	3.564381	0.003922	0.001786	3.214582
18	SWE1 BiSE2 100°	0.696054	0.04816	0.732528	0.070984	0.002907	3.066636
19	SWE2 BiSE1 10°	0.605904	0.047728	0.635775	0.053278	0.003053	3.037022
20	SWE1 BiSE1 160°	0.798603	0.03658	0.818047	0.030203	0.003271	3.010344
21	SWE4 BiSE1 40°	0.377457	0.040222	0.402865	0.046755	0.00351	2.992115
22	SWE4 BiSEPh 140°	0.950543	0.235496	1.080616	0.216896	0.003657	2.973277
23	USG1 BiSE1 160°	0.798603	0.03658	0.818896	0.035469	0.004424	2.909825
24	SWE3 BiSE3 10°	0.166226	0.074668	0.20712	0.071639	0.004711	2.888354
25	USG1 BiSE1 70°	0.827659	0.033827	0.844968	0.028402	0.004872	2.876521
26	USG1 BiSE1 120°	0.828745	0.033532	0.845538	0.027906	0.005641	2.826313
27	SWE4 BiSEPh 150°	0.979327	0.252761	1.108462	0.219873	0.00564	2.826213
28	SWE4 BiSE2 40°	0.061266	0.018073	0.072461	0.02235	0.005793	2.823696
29	USG1 BiSE2 120°	0.622579	0.075301	0.657216	0.051242	0.005978	2.809499
30	SWE4 BiSEPh 180°	1.592947	0.187638	1.691713	0.178056	0.006239	2.791569
31	SWE4 BiSE3 40°	0.018354	0.008952	0.023894	0.011514	0.007168	2.750298
32	SWE3 BiSE2 10°	0.244355	0.071159	0.279638	0.061776	0.00711	2.74549
33	SWE4 BiSE2 160°	0.061134	0.022445	0.073466	0.024045	0.00747	2.730234
34	SWE4 BiSE2 130°	0.062614	0.023268	0.076048	0.027428	0.007924	2.71165
35	SWE4 BiSEPh 110°	1.22281	0.244755	1.344901	0.220965	0.007828	2.711487
36	SWE3 BiSE3 120°	0.221181	0.064028	0.186699	0.068732	0.008767	2.673073
37	USG1 BiSE1 60°	0.82	0.039052	0.837438	0.02814	0.008788	2.671992
38	SWE4 BiSE2 120°	0.072569	0.030537	0.09246	0.044382	0.009236	2.663813
39	SWE3 BiSE1 120°	0.441628	0.061967	0.47698	0.07469	0.00961	2.642753
40	SWE4 BiSE3 130°	0.018883	0.013195	0.026117	0.014923	0.009639	2.639959
41	SWE3 BiSE1 110°	0.438941	0.06123	0.469725	0.061498	0.011026	2.588684
42	SWE4 BiSEPh 170°	1.169662	0.168885	1.254345	0.168976	0.011072	2.587085
43	USG2 BiSE1 10°	0.605904	0.047728	0.629652	0.047428	0.011393	2.576482
44	SWE3 BiSE2 110°	0.256161	0.056953	0.284259	0.056501	0.012009	2.55701
45	SWE1 BiSE1 20°	0.782564	0.035649	0.800779	0.038385	0.012894	2.531766
46	SWE4 BiSE3 120°	0.022366	0.017962	0.035399	0.032433	0.0138	2.522367

(Continues)

TABLE 5 (Continued)

		Group negative		Group positive			
N	Feature	Mean	SD	Mean	SD	*p*-value	*t*-value
47	SWE3 BiSEPh 120°	3.138986	0.324469	2.977761	0.338902	0.01385	2.50448
48	SWE4 BiSE3 160°	0.018184	0.012395	0.024257	0.012737	0.014316	2.491774
49	SWE1 BiSE2 160°	0.539504	0.103581	0.580482	0.065836	0.015216	2.471445
50	SWE4 BiSE3 110°	0.02777	0.020301	0.042398	0.03735	0.015924	2.467859
51	SWE3 BiSE1 10°	0.441871	0.081832	0.480681	0.081287	0.015701	2.456374
52	USG2 BiSEPh 150°	3.520828	0.065396	3.544804	0.03267	0.016676	2.442305
53	SWE1 BiSE1 40°	0.797144	0.037816	0.81404	0.034013	0.016667	2.432959
54	SWE2 BiSE3 110°	0.317734	0.069173	0.352125	0.076353	0.016953	2.428487
55	SWE3 BiSE3 110°	0.177436	0.067456	0.209352	0.069055	0.01768	2.411199
56	SWE4 BiSE1 120°	0.4278	0.045477	0.452427	0.058693	0.018351	2.401288
57	SWE4 BiSE3 100°	0.03642	0.024201	0.052047	0.040281	0.019222	2.390745
58	SWE4 BiSE2 110°	0.072942	0.030215	0.091148	0.047165	0.021703	2.340556
59	SWE4 BiSEPh 70°	0.969568	0.204163	1.05734	0.18412	0.02128	2.338077
60	SWE1 BiSEPh 100°	3.548975	0.02998	3.529635	0.051781	0.022923	2.321661
61	SWE4 BiSE3 180°	0.02818	0.014957	0.035943	0.019506	0.024568	2.285982
62	SWE4 BiSEPh 100°	2.302574	0.48042	2.493738	0.38448	0.024405	2.283925
63	SWE2 BiSE2 10°	0.413249	0.06847	0.445011	0.074554	0.02449	2.283828
64	SWE1 BiSEPh 140°	3.562154	0.007447	3.564936	0.005058	0.024549	2.283294
65	SWE4 BiSEPh 90°	1.217874	0.218661	1.319028	0.240488	0.02571	2.264418
66	USG1 BiSE1 140°	0.817562	0.027427	0.831099	0.033708	0.026201	2.258688
67	SWE4 BiSE3 80°	0.023004	0.014098	0.033369	0.029716	0.027436	2.253834
68	USG4 BiSE1 40°	0.377457	0.040222	0.396572	0.046966	0.027046	2.244849
69	SWE4 BiSE2 100°	0.08225	0.033138	0.101358	0.051686	0.027738	2.241153
70	USG3 BiSEPh 40°	3.30541	0.222354	3.198353	0.268701	0.028314	2.226783
71	SWE2 BiSE3 140°	0.347745	0.07387	0.313594	0.085154	0.030091	2.200977

Note: N indicates the feature rank, and the feature name is composed from the imaging method (B-mode SWE or USG) combined with the IMF value (1–4). BiSE indicates bi-spectrum entropy. The angle (x°) refers to the Radon transform angle. There are two mean and standard deviation (SD) columns, one for the positive group and the other for the negative group. The feature performance is summarized with *p*- and *t*- values.

Figure 6 shows the bispectrum magnitude plots of negative and positive classes (Chandran & Elgar, 1991, 1992, 1993; Nikias & Mendel, 1993; Vicnesh et al., 2020). It can be noted from this figure that the plots are unique, and that the signatures from plots have yielded higher classification performance.

Table 2 shows the classification results based on features extracted from B-mode ultrasound. The highest accuracy was 74.77%. Table 3 shows the classification performance results obtained using SWE images. These results indicate an accuracy of 87.85%. Fusing features extracted from both ultrasound imaging modalities, we achieved an accuracy of 89.72%, as shown in Table 4. This indicates that data fusion improved the ALN detection performance. Having these clear results translates into the following advantages of the proposed system:

1. To the best of our knowledge this is the first work to use B-mode USG and SWE for automated detection of ALNs.
2. Obtained higher classification accuracy (ACC 89.72%) and specificity (94.74%).
3. Combination of BEMD and HOS entropies have yielded highest classification performance.
4. Proposed model is accurate and robust as we have used 10-fold cross-validation.
5. Proposed unique bispectrum magnitude plots for two classes.

Limitations of this work are as follows:

1. In this work, we used 107 images (57 negative and 50 positive). That small number of images might be insufficient to represent the variations of ultrasound images encountered in a clinical setting. Furthermore, that number of images is not sufficient to train and test deep learning models (Faust, Hagiwara, et al., 2018).

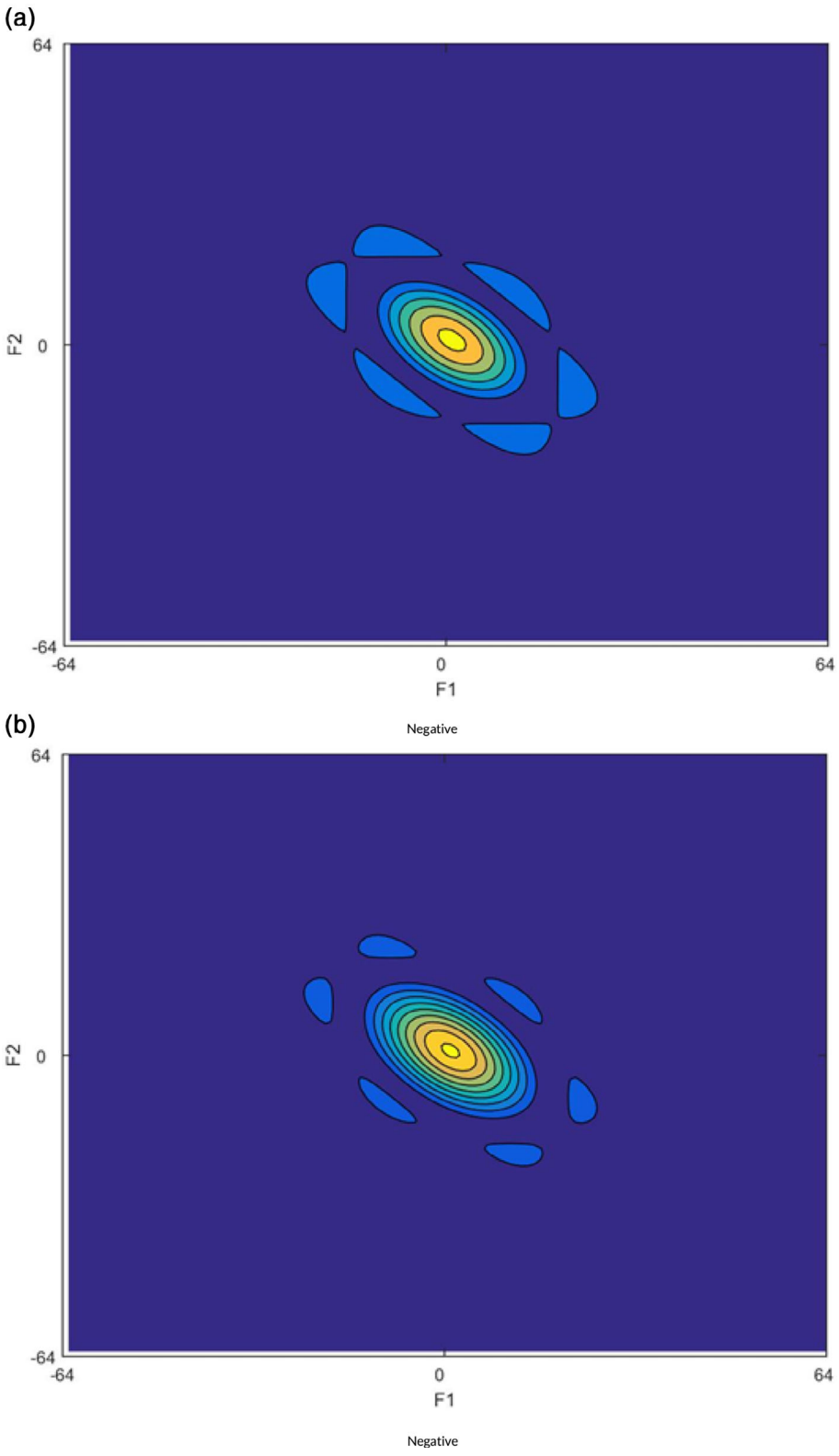

FIGURE 6 Bispectrum magnitude plots obtained from SWE images: (a) negative and (b) positive

2. The PNN classifier uses a large amount of memory, and it needs a proper smoothing parameter to achieve peak performance.

In the future, we intend to extend this work using more images, and also to explore the possibility of detecting other types of cancers like thyroid, ovarian carcinoma, and other diseases such as liver cirrhosis.

5 | CONCLUSION

In this study, we investigated image acquisition and processing methods that can be used to improve the diagnostic relevance of ultrasound scans for ALN metastasis detection. To facilitate the study, we constructed a sophisticated information extraction system. That system takes B-mode USG and SWE imagery from the ALN as input. Based on a specific input image, the system indicates if it shows signs of metastasis (positive) or not (negative). The generated labels were compared with the ground truth established by experienced human radiologists. The result of this comparison was reported in terms of ACC, SEN, SPE, and PPV. Our study was driven by the hypothesis that ultrasound imagery, captured with current technology, contains sufficient information to improve ALN metastasis detection. To test this hypothesis, we have used the proposed information extraction system to generate labels from SWE and B-mode USG ultrasound imagery. In a configuration that incorporated PNN, the information extraction system achieved an accuracy of 73.83% for discriminating positive versus negative cases based on B-mode USG imagery. With the same configuration, the system achieved 87.85% ACC for SWE imagery. This indicates that SWE images hold more diagnostically relevant information. In a last test, we combined the features extracted from both B-mode USG and SWE images to determine the diagnostic relevance of combining data from multiple sources. This test resulted in the best classification accuracy of 89.72%. From a data science perspective, these results make sense because combining the information from different data sources usually leads to better results. Having improved non-invasive methods to support the diagnosis of ALN metastasis might lead to a lower number of invasive diagnostic support tests. Lowering the number of invasive tests can reduce the risk for patients and improve overall outcome.

ACKNOWLEDGEMENTS

This study was supported by University of Malaya Faculty Research Grant (RU Grant-Faculty Programme (Project No: GPF06C-2018) and Fundamental Research Grant Scheme (Project No: FP017-2019A) and facilitated by the University of Malaya Research Imaging Centre (UMRIC).

DATA AVAILABILITY STATEMENT

Author elects to not share data.

ACRONYMS

ACC Accuracy
ACR American College of Radiology
ALN Axillary lymph node
ALND Axillary lymph node dissection
BEMD Bi-dimensional empirical mode decomposition
DT Decision tree
FN False negative
FP False positive
HOS Higher order spectra
IMF Intrinsic mode functions
K-NN K-nearest neighbour
LDA Linear discriminant analysis
NoF Number of features
PNN Probabilistic neural network
PPV Positive predictive value
QDA Quadratic discriminant analysis
RBF Radial basis function
ROI Region of interest
SEN Sensitivity
SLNB Sentinel lymph node biopsy
SPE Specificity
SWE Shear wave elastography
SVM Support vector machine
TN True negative
TP True positive
UMMC University Malaya Medical Centre
US Ultrasound
USG Ultrasonography

ORCID

Oliver Faust https://orcid.org/0000-0002-3979-4077
Nazimah Ab Mumin https://orcid.org/0000-0001-8720-5700
U. Rajendra Acharya https://orcid.org/0000-0003-2689-8552

REFERENCES

Acharya, U. R., Meiburger, K. M., Faust, O., Koh, J. E. W., Oh, S. L., Ciaccio, E. J., Subudhi, A., Jahmunah, V., & Sabut, S. (2019). Automatic detection of ischemic stroke using higher order spectra features in brain MRI images. *Cognitive Systems Research*, *58*, 134–142.

Acharya, U. R., Meiburger, K. M., Koh, J. E. W., Hagiwara, Y., Oh, S. L., Leong, S. S., Ciaccio, E. J., Wong, J. H. D., Shah, M. N. M., Molinari, F., & Molinari, F. (2019). Automated detection of chronic kidney disease using higher-order features and elongated quinary patterns from b-mode ultrasound images. *Neural Computing and Applications*, *32*, 1–10.

Acharya, U. R., Ng, W. L., Rahmat, K., Sudarshan, V. K., Koh, J. E., Tan, J. H., Hagiwara, Y., Yeong, C. H., & Ng, K. H. (2017). Data mining framework for breast lesion classification in shear wave ultrasound: A hybrid feature paradigm. *Biomedical Signal Processing and Control*, *33*, 400–410.

Acharya, U. R., Raghavendra, U., Fujita, H., Hagiwara, Y., Koh, J. E., Hong, T. J., Sudarshan, V. K., Vijayananthan, A., Yeong, C. H., Gudigar, A., & Gudigar, A. (2016). Automated characterization of fatty liver disease and cirrhosis using curvelet transform and entropy features extracted from ultrasound images. *Computers in Biology and Medicine*, *79*, 250–258.

Acharya, U. R., Sree, S. V., Swapna, G., Martis, R. J., & Suri, J. S. (2013). Automated EEG analysis of epilepsy: A review. *Knowledge-Based Systems*, *45*, 147–165.

Acharya, U. R., Sudarshan, V. K., Koh, J. E., Martis, R. J., Tan, J. H., Oh, S. L., Muhammad, A., Hagiwara, Y., Mookiah, M. R. K., Chua, K. P., Chua, C. K., & Chua, K. P. (2017). Application of higher-order spectra for the characterization of coronary artery disease using electrocardiogram signals. *Biomedical Signal Processing and Control*, *31*, 31–43.

Altman, N. S. (1992). An introduction to kernel and nearest-neighbor nonparametric regression. *The American Statistician*, *46*(3), 175–185.

Alvarez, S., Añorbe, E., Alcorta, P., López, F., Alonso, I., & Cortés, J. (2006). Role of sonography in the diagnosis of axillary lymph node metastases in breast cancer: A systematic review. *American Journal of Roentgenology*, *186*(5), 1342–1348.

Amanti, C., Lombardi, A., Maggi, S., Moscaroli, A., Lo Russo, M., Maglio, R., Provenza, G., Romano, C., Pezzatini, M., Scopinaro, F., & di Stefano, D. (2009). Is complete axillary dissection necessary for all patients with positive findings on sentinel lymph node biopsy? Validation of a breast cancer nomogram for predicting the likelihood of a non-sentinel lymph node. *Tumori Journal*, *95*(2), 153–155.

American College of Radiology and D'Orsi, Carl J. (2013). *ACR BI-RADS Atlas: Breast imaging reporting and data system; mammography, ultrasound, magnetic resonance imaging, follow-up and outcome monitoring, data dictionary*. American College of Radiology.

Balakrishnama, S., & Ganapathiraju, A. (1998). Linear discriminant analysis-a brief tutorial. In *Institute for signal and information processing* (Vol. *18*, pp. 1–8).

Berg, W. A., Cosgrove, D. O., Doré, C. J., Schäfer, F. K., Svensson, W. E., Hooley, R. J., Ohlinger, R., Mendelson, E. B., Balu-Maestro, C., Locatelli, M., Tourasse, C., Cavanaugh, B. C., Juhan, V., Stavros, A. T., Tardivon, A., Gay, J., Henry, J.-P., Cohen-Bacrie, C., & For the BE1 Investigators. (2012). Shear-wave elastography improves the specificity of breast US: The BE1 multinational study of 939 masses. *Radiology*, *262*(2), 435–449.

Chandran, V., Carswell, B., Boashash, B., & Elgar, S. (1997). Pattern recognition using invariants defined from higher order spectra: 2-d image inputs. *IEEE Transactions on Image Processing*, *6*(5), 703–712.

Chandran, V. & Elgar, S. (1991). Shape Discrimination Using Invariants Defined from Higher-Order Spectra. Paper presented at the Acoustics, Speech, and Signal Processing, IEEE International Conference, Toronto, Ont., Canada; pp. 3105–3106.

Chandran, V. & Elgar, S. L. (1992). Position, Rotation, and Scale Invariant Recognition of Images Using Higher-Order Spectra. Paper presented at the Acoustics, Speech, and Signal Processing, IEEE International Conference, Toronto, Ont., Canada; (Vol. 5, pp. 213–216).

Chandran, V., & Elgar, S. L. (1993). Pattern recognition using invariants defined from higher order spectra-one-dimensional inputs. *IEEE Transactions on Signal Processing*, *41*(1), 205–212.

Chen, C.-S., & Jeng, Y. (2014). Two-dimensional nonlinear geophysical data filtering using the multidimensional eemd method. *Journal of Applied Geophysics*, *111*, 256–270.

Choi, J. J., Kang, B. J., Kim, S. H., Lee, J. H., Jeong, S. H., Yim, H. W., Song, B. J., & Jung, S. S. (2011). Role of sonographic elastography in the differential diagnosis of axillary lymph nodes in breast cancer. *Journal of Ultrasound in Medicine*, *30*(4), 429–436.

Chua, K. C., Chandran, V., Acharya, U. R., & Lim, C. M. (2010). Application of higher order statistics/spectra in biomedical signals—A review. *Medical Engineering & Physics*, *32*(7), 679–689.

Cortes, C., & Vapnik, V. (1995). Support-vector networks. *Machine Learning*, *20*(3), 273–297.

Coster, M., & Chermant, J.-L. (2001). Image analysis and mathematical morphology for civil engineering materials. *Cement and Concrete Composites*, *23*(2–3), 133–151.

Coutant, C., Olivier, C., Lambaudie, E., Fondrinier, E., Marchal, F., Guillemin, F., Seince, N., Thomas, V., Lévêque, J., Barranger, E., Darai, E., Uzan, S., Houvenaeghel, G., & Rouzier, R. (2009). Comparison of models to predict nonsentinel lymph node status in breast cancer patients with metastatic sentinel lymph nodes: A prospective multicenter study. *Journal of Clinical Oncology*, *27*(17), 2800–2808.

della Rovere, G. Q., Bonomi, R., Ashley, S., & Benson, J. (2006). Axillary staging in women with small invasive breast tumours. *European Journal of Surgical Oncology*, *32*(7), 733–737.

Ecanow, J. S., Abe, H., Newstead, G. M., Ecanow, D. B., & Jeske, J. M. (2013). Axillary staging of breast cancer: What the radiologist should know. *Radiographics*, *33*(6), 1589–1612.

Evans, A., Rauchhaus, P., Whelehan, P., Thomson, K., Purdie, C. A., Jordan, L. B., Michie, C. O., Thompson, A., & Vinnicombe, S. (2014). Does shear wave ultrasound independently predict axillary lymph node metastasis in women with invasive breast cancer? *Breast Cancer Research and Treatment*, *143*(1), 153–157.

Evans, A., Whelehan, P., Thomson, K., Brauer, K., Jordan, L., Purdie, C., McLean, D., Baker, L., Vinnicombe, S., & Thompson, A. (2012). Differentiating benign from malignant solid breast masses: Value of shear wave elastography according to lesion stiffness combined with greyscale ultrasound according to bi-rads classification. *British Journal of Cancer*, *107*(2), 224–229.

Faust, O., Acharya, U. R., Meiburger, K. M., Molinari, F., Koh, J. E., Yeong, C. H., Kongmebhol, P., & Ng, K. H. (2018). Comparative assessment of texture features for the identification of cancer in ultrasound images: A review. *Biocybernetics and Biomedical Engineering*, *38*(2), 275–296.

Faust, O., Hagiwara, Y., Hong, T. J., Lih, O. S., & Acharya, U. R. (2018). Deep learning for healthcare applications based on physiological signals: A review. *Computer Methods and Programs in Biomedicine*, *161*, 1–13.

Fernández, A. G., Fraile, M., Giménez, N., Reñe, A., Torras, M., Canales, L., Torres, J., Barco, I., González, S., Veloso, E., González, C., Cirera, L., & Pessarrodona, A. (2011). Use of axillary ultrasound, ultrasound-fine needle aspiration biopsy and magnetic resonance imaging in the preoperative triage of breast cancer patients considered for sentinel node biopsy. *Ultrasound in Medicine & Biology*, *37*(1), 16–22.

Giuliano, A. E., Hunt, K. K., Ballman, K. V., Beitsch, P. D., Whitworth, P. W., Blumencranz, P. W., Leitch, A. M., Saha, S., McCall, L. M., & Morrow, M. (2011). Axillary dissection vs no axillary dissection in women with invasive breast cancer and sentinel node metastasis: A randomized clinical trial. *JAMA*, *305*(6), 569–575.

Goldhirsch, A., Wood, W. C., Coates, A. S., Gelber, R. D., Thürlimann, B., Senn, H.-J., & Members, P. (2011). Strategies for subtypes—Dealing with the diversity of breast cancer: Highlights of the st gallen international expert consensus on the primary therapy of early breast cancer 2011. *Annals of Oncology*, *22*(8), 1736–1747.

Huang, N. E., Shen, Z., Long, S. R., Wu, M. C., Shih, H. H., Zheng, Q., Yen, N. C., Tung, C. C., & Liu, H. H. (1998). The empirical mode decomposition and the hilbert spectrum for nonlinear and non-stationary time series analysis. *Proceedings of the Royal Society of London Series A: Mathematical, Physical and Engineering Sciences*, *454*(1971), 903–995.

Izenman, A. J. (2013). Linear discriminant analysis. In *Modern multivariate statistical techniques* (pp. 237–280). Springer.

Kilic, F., Velidedeoglu, M., Ozturk, T., Kandemirli, S. G., Dikici, A. S., Er, M. E., Aydogan, F., Kantarci, F., & Yilmaz, M. H. (2016). Ex vivo assessment of sentinel lymph nodes in breast cancer using shear wave elastography. *Journal of Ultrasound in Medicine*, *35*(2), 271–277.

Koh, J. E., Acharya, U. R., Hagiwara, Y., Raghavendra, U., Tan, J. H., Sree, S. V., Bhandary, S. V., Rao, A. K., Sivaprasad, S., Chua, K. C., Laude, A., & Tong, L. (2017). Diagnosis of retinal health in digital fundus images using continuous wavelet transform (CWT) and entropies. *Computers in Biology and Medicine*, *84*, 89–97.

Kohavi, R. (1995). A Study of Cross-Validation and Bootstrap for Accuracy Estimation and Model Selection. Paper presented at the IJCAI, Toronto, Ont., Canada; (Vol. 14, pp. 1137–1145).

Kramer, O. (2013). K-nearest neighbors. In *Dimensionality reduction with unsupervised nearest neighbors* (pp. 13–23). Springer.

Lee, B., Lim, A. K., Krell, J., Satchithananda, K., Coombes, R. C., Lewis, J. S., & Stebbing, J. (2013). The efficacy of axillary ultrasound in the detection of nodal metastasis in breast cancer. *American Journal of Roentgenology*, *200*(3), W314–W320.

Loh, W.-Y. (2011). Classification and regression trees. *Wiley Interdisciplinary Reviews: Data Mining and Knowledge Discovery*, *1*(1), 14–23.

Luo, S., Yao, G., Hong, Z., Zhang, S., Wang, W., Zhang, J., Zhang, Y., Wu, J., Zhang, L., Cheng, H., Hao, Y., & Li, Y. (2019). Qualitative classification of shear wave elastography for differential diagnosis between benign and metastatic axillary lymph nodes in breast cancer. *Frontiers in Oncology*, *9*, 533.

Mainiero, M. B., Cinelli, C. M., Koelliker, S. L., Graves, T. A., & Chung, M. A. (2010). Axillary ultrasound and fine-needle aspiration in the preoperative evaluation of the breast cancer patient: An algorithm based on tumor size and lymph node appearance. *American Journal of Roentgenology*, *195*(5), 1261–1267.

Mohebali, B., Tahmassebi, A., Meyer-Baese, A., & Gandomi, A. H. (2020). Probabilistic neural networks: A brief overview of theory, implementation, and application. In *Handbook of probabilistic models* (pp. 347–367). Elsevier.

Mozaffarilegha, M., Yaghobi Joybari, A., & Mostaar, A. (2020). Medical image fusion using bi-dimensional empirical mode decomposition (BEMD) and an efficient fusion scheme. *Journal of Biomedical Physics & Engineering*, *10*(6), 727.

Murtaugh, P. A. (2014). In defense of p values. *Ecology*, *95*(3), 611–617.

Ng, W. L., Omar, N., Ab Mumin, N., Hamid, M. T. R., Vijayananthan, A., & Rahmat, K. (2021). Diagnostic accuracy of shear wave elastography as an adjunct tool in detecting axillary lymph nodes metastasis. *Academic Radiology*. https://www.sciencedirect.com/science/article/pii/S1076633221001380

Ng, W. L., Rahmat, K., Fadzli, F., Rozalli, F. I., Mohd-Shah, M. N., Chandran, P. A., Westerhout, C. J., Vijayananthan, A., & Aziz, Y. F. A. (2016). Shearwave elastography increases diagnostic accuracy in characterization of breast lesions. *Medicine*, *95*(12), e3146.

Nikias, C. L., & Mendel, J. M. (1993). Signal processing with higher-order spectra. *IEEE Signal Processing Magazine*, *10*(3), 10–37.

Noble, W. S. (2006). What is a support vector machine? *Nature Biotechnology*, *24*(12), 1565–1567.

Noronha, K. P., Acharya, U. R., Nayak, K. P., Martis, R. J., & Bhandary, S. V. (2014). Automated classification of glaucoma stages using higher order cumulant features. *Biomedical Signal Processing and Control*, *10*, 174–183.

Nunes, J. C., Guyot, S., & Deléchelle, E. (2005). Texture analysis based on local analysis of the bidimensional empirical mode decomposition. *Machine Vision and Applications*, *16*(3), 177–188.

Olgun, D. Ç., Korkmazer, B., Kılıç, F., Dikici, A. S., Velidedeoğlu, M., Aydoğan, F., Kantarcı, F., & Yılmaz, M. H. (2014). Use of shear wave elastography to differentiate benign and malignant breast lesions. *Diagnostic and Interventional Radiology*, *20*(3), 239–244.

Pardoe, I., Yin, X., & Cook, R. D. (2007). Graphical tools for quadratic discriminant analysis. *Technometrics*, *49*(2), 172–183.

Pizer, S. M., Amburn, E. P., Austin, J. D., Cromartie, R., Geselowitz, A., Greer, T., Romeny, B. H., Zimmerman, J. B., & Zuiderveld, K. (1987). Adaptive histogram equalization and its variations. *Computer Vision, Graphics, and Image Processing*, *39*(3), 355–368.

Radon, J. (1986). On the determination of functions from their integral values along certain manifolds. *IEEE Transactions on Medical Imaging*, *5*(4), 170–176.

Rokach, L., & Maimon, O. (2005). Decision trees. In *Data mining and knowledge discovery handbook* (pp. 165–192). Springer.

Saravanan, C. (2010). *Color Image to Grayscale Image Conversion*. Paper presented at the 2010 Second International Conference on Computer Engineering and Applications (Vol. 2, pp. 196–199).

Seo, M., & Sohn, Y.-M. (2018). Differentiation of benign and metastatic axillary lymph nodes in breast cancer: Additive value of shear wave elastography to b-mode ultrasound. *Clinical Imaging*, *50*, 258–263.

Siegel, R. L., Miller, K. D., & Jemal, A. (2019). Cancer statistics, 2019. *CA: A Cancer Journal for Clinicians*, *69*(1), 7–34.

Srivastava, S., Gupta, M. R., & Frigyik, B. A. (2007). Bayesian quadratic discriminant analysis. *Journal of Machine Learning Research*, *8*, 1277–1305.

Student. (1908). The probable error of a mean. *Biometrika*, *6*, 1–25.

Tamaki, K., Tamaki, N., Kamada, Y., Uehara, K., Miyashita, M., Chan, M. S., Ishida, T., Ohuchi, N., & Sasano, H. (2013). Non-invasive evaluation of axillary lymph node status in breast cancer patients using shear wave elastography. *The Tohoku Journal of Experimental Medicine*, *231*(3), 211–216.

Tamaki, K., Tamaki, N., Kamada, Y., Uehara, K., Miyashita, M., Ishida, T., & Sasano, H. (2013). A non-invasive modality: The US virtual touch tissue quantification (VTTQ) for evaluation of breast cancer. *Japanese Journal of Clinical Oncology*, *43*(9), 889–895.

Tourasse, C., Dénier, J. F., Awada, A., Gratadour, A.-C., Nessah-Bousquet, K., & Gay, J. (2012). Elastography in the assessment of sentinel lymph nodes prior to dissection. *European Journal of Radiology*, *81*(11), 3154–3159.

Van la Parra, R., Ernst, M., Bevilacqua, J., Mol, S., Van Zee, K., Broekman, J., & Bosscha, K. (2009). Validation of a nomogram to predict the risk of nonsentinel lymph node metastases in breast cancer patients with a positive sentinel node biopsy: Validation of the mskcc breast nomogram. *Annals of Surgical Oncology*, *16*(5), 1128–1135.

Vicnesh, J., Wei, J. K. E., Oh, S. L., Arunkumar, N., Abdulhay, E. W., Ciaccio, E. J., & Acharya, U. R. (2020). Autism spectrum disorder diagnostic system using hos bispectrum with EEG signals. *International Journal of Environmental Research and Public Health*, *17*(3), 971.

Wu, M., & Burstein, D. E. (2004). Fine needle aspiration. *Cancer Investigation*, *22*(4), 620–628.

Xanthopoulos, P., Pardalos, P. M., & Trafalis, T. B. (2013). Linear discriminant analysis. In *Robust data mining* (pp. 27–33). Springer.

Youk, J. H., Son, E. J., Kim, J.-A., & Gweon, H. M. (2017). Pre-operative evaluation of axillary lymph node status in patients with suspected breast cancer using shear wave elastography. *Ultrasound in Medicine & Biology*, *43*(8), 1581–1586.

AUTHOR BIOGRAPHIES

The-Hanh Pham received the B.E. degree in Electronics and Telecommunications Engineering from Hanoi University of Science and Technology, Vietnam, in 2001. At National University of Singapore (NUS), he earned the Ph.D. degree in Electrical and Computer Engineering in 2008. He was a Research Fellow with NUS and a Scientist with the Institute for Infocomm Research (I2R), Singapore. He is now a Lecturer in School of Engineering, Ngee Ann Polytechnic, Singapore. His current research interests are in machine learning and its applications in biomedical engineering.

Oliver Faust is a senior faculty member at Sheffield Hallam University, UK. He received his Ph.D. from Aberdeen University (UK), DEng from Chiba University (Japan), and Dipl.-Ing (FH) from the private university of applied science Dieburg, Germany. He has published more than 100 papers, in refereed international SCI-IF journals (91), international conference proceedings (21), book chapters (6) with more than 4900 citations in Google Scholar (with h-index of 32). He has worked on various funded projects, with grants worth more than 1 million £. He serves as an associate editor for Computer Methods and Programs in Biomedicine. He is on the editorial board of Computers in Biology and Medicine, Biomedical Signal Processing (specialty section of Frontiers in Signal Processing), MDPI signals, and MDPI International Journal of Environmental Research and Public Health. He has served as Guest Editor for many journals.

Joel En Wei Koh received the B.Eng. (Biomedical) degree from Singapore University of Social Sciences and the M.Sc. degree from Nanyang Technological University, Singapore. He is currently a Researcher with Ngee Ann Polytechnic, Singapore. He has published more than 33 journal papers in the past 5 years. His principal interests include artificial intelligence, biomedical imaging, and machine learning. Please visit https://www.researchgate.net/profile/Joel_En_Wei_Koh for more information.

Edward J. Ciaccio received the M.S. and Ph.D. degrees from Rutgers University, Department of Biomedical Engineering. He is currently a Senior Research Scientist with the Department of Medicine, Division of Cardiology, and with the Celiac Disease Center, Columbia University, and also an Honorary Principal Research Fellow with the Department of Medicine, Division of Cardiology, Imperial College London. He has published 200 peer-reviewed articles on such topics as biomedical signal processing of heart electrograms, and image processing of villous atrophy in celiac disease patients. In computational biology, he has developed biophysical models of activation wavefront propagation for ventricular tachycardia and for atrial fibrillation. His work received a Paper of the Year Award from Heart Rhythm journal, one of the leading publications in cardiac electrophysiology, an Established Investigator Award from the American Heart Association, a Whitaker Foundation Research Award, and four United States patents. He is Editor-In-Chief of Informatics in Medicine Unlocked.

Prabal Datta Barua obtained Ph.D. (Information System) from the University of Southern Queensland. He is an academic and accredited research supervisor at the University of Southern Queensland with 15 years of teaching experience. Dr Barua received research support from the Queensland Government Innovation Connections under the Entrepreneurs program to research "Cancer Recurrence Using Innovative Machine Learning Approaches". Dr Barua is interested in AI technology development in health, education, agriculture, and environmental science and published several papers in the Q1 journal. He is an industry leader in ICT entrepreneurship in Australia and sitting as an ICT advisory panel member of many organisations. Dr Barua is an Adjunct Professor at the University of Southern Queensland and an Honourary Industry Fellow at the University of Technology Sydney.

Norlia Omar obtained her medical degree (MBBS) in 2011 from University Malaya. Previously she has served in Hospital Taiping as a medical officer in Radiology Department from 2016 to 2017. Currently she is a radiology trainee undergoing Master of Radiology (M.Rad) in University Malaya Medical Centre.

Ng Wei Lin joined as an academic staff in the Department of Biomedical Imaging, University Malaya in 2018. She obtained her medical degree (MBBS) and masters of radiology (MRad) from University of Malaya. Previously she has served in Hospital Taiping as a radiologist from 2016 to 2017. She is currently pursuing her fellowship in interventional radiology with special interest in women's health. Her past research includes shear wave ultrasound in breast lesions. She has published 16 papers with h-index of 5. She currently has a national grant for BREOMICS (BREast radiOMICS): Deciphering Radiomics Signatures of Breast Cancer.

Nazimah Ab Mumin M.BChB., M.Rad., F.R.C.R., A.M.M., is a medical lecturer and clinical radiologist at Universiti Teknologi MARA, Malaysia. She is a breast imaging radiologist at UiTM Specialist Medical Centre, Hospital UiTM Puncak Alam and UiTM Private Specialist Centre. She obtained her Clinical Fellowship in Breast Imaging from University of Malaya Medical Centre. Her current grants and research projects are on MRI Breast, Automated Breast Ultrasound, Digital Breast Tomosynthesis and Radiomics. https://scholar.google.com/citations?hl=en&user=IgFYtUQAAAAJ

Kartini Rahmat M.B.B.S., F.R.C.R., M.Rad(Mal)., E.B.B.I., is a Clinical Professor and Radiology Consultant at the Biomedical Imaging, University of Malaya, Kuala Lumpur. She obtained post-graduate qualifications from University of Malaya and furthered subspeciality training in Royal Perth Hospital (Aust) and Queensquare Hospital London, UK. Her clinical interests and research contributions are focused on Breast Imaging, Neuroradiology, Informatics and advanced MRI/Ultrasound applications. Dr Kartini currently serves as unit head of University of Malaya Research Imaging Centre. She has published more than 100 academic articles, mostly refereed international journals (80), and international conference proceedings (with h-index of 17 on WOS/Publons). She is working on multiple funded academic clinical and industry projects and PI holder for breast oncology, cancer radiomics, neurodegenerative disease and epilepsy disorders.

Udyavara Rajendra Acharya M.Tech., Ph.D., D.Eng., D.Sc. is a senior faculty member at Ngee Ann Polytechnic, Singapore. He is also (i) Adjunct Professor at University of Malaya, Malaysia, (ii) Adjunct Professor at Asia University, Taiwan, (iii) Associate faculty at Singapore University of Social Sciences, Singapore and (iv) Adjunct Professor at University of Southern Queensland, Australia. He received his Ph.D. from National Institute of Technology Karnataka (Surathkal, India), DEng from Chiba University (Japan) and DSc from AGH University of Science and Technology, Poland. He has published more than 500 papers, in refereed international SCI-IF journals (345), international conference proceedings (42), books (17) with more than 48,000 citations in Google Scholar (with h-index of 112). He has worked on various funded projects, with grants worth more than 6 million SGD. He is ranked in the top 1% of the Highly Cited Researchers for the last five consecutive years (2016 to 2020) in Computer Science according to the Essential Science Indicators of

Thomson. He is on the editorial board of many journals and has served as Guest Editor for many journals. Please visit https://scholar.google.com.sg/citations?user=8FjY99sAAAAJ&hl=en for more details.

How to cite this article: Pham, T.-H., Faust, O., Koh, J. E. W., Ciaccio, E. J., Barua, P. D., Omar, N., Ng, W. L., Ab Mumin, N., Rahmat, K., & Acharya, U. R. (2022). Fusion of B-mode and shear wave elastography ultrasound features for automated detection of axillary lymph node metastasis in breast carcinoma. *Expert Systems*, e12947. https://doi.org/10.1111/exsy.12947